Nanoscale

On Interfacial Viscosity in Nanochannels

Journal:	*Nanoscale*
Manuscript ID	NR-ART-03-2020-002294.R1
Article Type:	Paper
Date Submitted by the Author:	09-May-2020
Complete List of Authors:	Nazari, Masoumeh; University of Houston System, Department of Mechanical Engineering Davoodabadi, Ali; University of Houston, Mechanical Engineering Huang, Dezhao; University of Notre Dame, Aerospace and Mechanical Engineering Luo, Tengfei; University of Notre Dame, Aerospace and Mechanical Engineering Ghasemi, Hadi; University of Houston System, Mechanical Engineering

SCHOLARONE™
Manuscripts

On Interfacial Viscosity in Nanochannels

Masoumeh Nazari[1,‡], Ali Davoodabadi[1,‡], Dezhao Huang[2], Tengfei Luo[2,*], and Hadi Ghasemi[1,*]

[1]Department of Mechanical Engineering, University of Houston, 4726 Calhoun Rd, Houston, Texas 77204, USA

[2]Department of Aerospace and Mechanical Engineering, University of Notre Dame, Notre Dame, Indiana 46556, USA

[‡]Equal Contributor

*Corresponding authors

KEYWORDS: interfacial viscosity, capillary motion, nanochannel.

ABSTRACT: Capillary driven transport of liquids in nanoscopic channels is an omnipresent phenomenon in nature and technology including fluid flow in human body and plants, drug delivery, nanofluidics devices, and energy/water systems. However, the kinetics of this mass transport mechanism remains in question as the well-known Lucas-Washburn (LW) model predicts significantly faster flow rates compared to the experimental observations. We here demonstrated the role of interfacial viscosity in capillary motion slowdown in nanochannels through a combination of experimental, analytical and molecular dynamics techniques. We showed that the slower liquid flow is due to the formation of a thin liquid layer adjacent to the channel walls with a viscosity substantially greater than the bulk liquid. By incorporating the effect of the interfacial layer, we presented a theoretical model that accurately predicts the capillarity kinetics in nanochannels of different heights. Non-equilibrium molecular dynamic simulation confirmed the obtained interfacial viscosities. The viscosities of isopropanol and ethanol within the interfacial layer were 9.048 mPa.s and 4.405 mPa.s, respectively (i.e. 279% and 276% greater than their bulk values). We also demonstrated that the interfacial layers are 6.4 nm and 5.3 nm-thick for isopropanol and ethanol, respectively.

Introduction

The spontaneous filling of conduits with small volume to surface ratio with a wetting liquid is called the capillarity effect (also known as capillary motion). Capillary motion is the underlying mechanism for mass transport in many natural systems such as the capillary rise of water and nutrients through plants xylems [1, 2, 3, 4], transport of water from aquifer to surface [5, 6] and the functioning of sweating glands in human body [7]. Also, capillarity plays a critical role in different microscale applications such as drug delivery [8], chemical analysis [9] and microfluidics and energy storage devices [10, 11, 12, 13]. However, capillarity in nanoscopic channels/tubes has recently gained substantial attention due to simplicity in its operation, generating reasonably high flow rates and possessing length scales comparable to ranges of intermolecular interactions. Proton-exchange membrane full cells [14], thermal management systems of electronics/photonics [15, 16, 17, 18, 19, 20], nanostructured material fabrication [15, 21], shale gas/oil production [22], water desalination [23, 3] and molecular separation [24, 25, 26] are only a few examples where capillary filling in nanochannels plays an essential role. Hence, understanding the physics of capillary motion in nanoscopic conduits is a necessity for analysis of the pertinent natural phenomena and enhancement of the related technological applications.

Lucas and Washburn are widely recognized to have proposed the first quantitative analyses of the capillarity kinetics in cylindrical capillaries through a relationship later named Lucas-Washburn (LW) equation that gives the liquid front position (x) with time (t) [27, 28]:

$$x = K\sqrt{t} \tag{1a}$$

$$K = \sqrt{r\gamma\cos\theta/2\mu} \tag{1b}$$

where r is the capillary radius, γ is the liquid surface tension, θ is the liquid/channel advancing contact angle and μ represents the liquid viscosity. The LW equation coefficient K can be modified for 2D channels (i.e. width much higher than the depth) with rectangular cross sections and a height of h as

$$K = \sqrt{h\gamma\cos\theta/3\mu} \tag{1c}$$

LW equation has been widely applied and verified for liquid capillary flow characterization in microchannels, but significant deviations are reported when compared against flow kinetics in nanochannels [29]. In fact, liquids fill nanochannels significantly slower than that predicted by LW equation, while still complying with the $x \propto \sqrt{t}$ relationship [30, 31, 32, 33, 34, 35, 36, 37, 38, 39]. Different studies have held a variety of physical phenomena responsible for the observed reduction in K. The electro-viscous effects [34, 36, 37], formation of gas nanobubbles [35, 40], variable dynamic contact angle at the liquid/channel wall interface [38], molecular structuring and formation of a stagnant liquid layer adjacent to the walls [39, 41, 42, 43] and chemical selectivity of the nanochannels toward specific liquids [32] are the main factors postulated to result in slowdown of the capillarity in nanoscale channels.

The electro-viscous effect in nanoscopic confined flows is caused by the presence of the electrical double layer near the

liquid/wall interface. The electro-viscous effect can increase the apparent dynamic viscosity due to the electroosmotic counter flow induced by a streaming potential and lead to filling slowdown. However, it has been shown that even the maximum possible contribution of the electro-viscous effect cannot result in filling speeds as small as those observed in the experiments [44, 45]. In fact, the electro-viscous effect is not sufficiently strong to account for the observed nanoscale capillary flow slowdown. Formation of nanobubbles in front of the advancing meniscus can slow down the imbibition by increasing the viscous resistance against the liquid flow. Notwithstanding, the bubble formation effect on capillary flow rate seems negligible in sub-100 nm channels [40]. Eq. (1b) shows that variations in the advancing contact angle between the liquid and wall can directly influence the penetration rate in nanochannels. The liquid penetration rate depends on the net force exerted on the liquid column from different existing forces including the capillary force, the inertial drag force and the viscous force. In fact, LW equation is derived based on the balance between the capillary and viscous forces. Hence, LW equation will not hold in the early stages of liquid wicking when inertial forces are dominant. Nonetheless, the inertia dominant regime has been shown to last for very limited time (less than 1 ns) and so cannot be responsible for the persistently slow capillary motion in nanochannels [46].

Thus, current literature is still incapable of identifying the mechanism(s) responsible for the capillary flow slowdown in nanoscopic conduits. The strong liquid/wall interactions in nanochannels can lead to formation of ultra-thin stagnant liquid layers on the solid surface which can reduce the effective height of the channel and results in increased flow resistance. For example, an ice-like hydration layer can be formed by reorientation and ordering of two to three layers of water molecules due to the strong water/wall interactions in hydrophilic channels [47].

An appropriate model can be developed by assuming that the molecular interactions at the liquid/wall interface lead to physical properties of a molecularly thin liquid layer adjacent to the wall to be different from that in the bulk. Here, we elucidate the role of interfacial viscosity in capillary motion in nanochannels. We also demonstrate that by including the interfacial viscosity effect in LW equation, it can be applied to predict the kinetics of capillary motion in nanochannels.

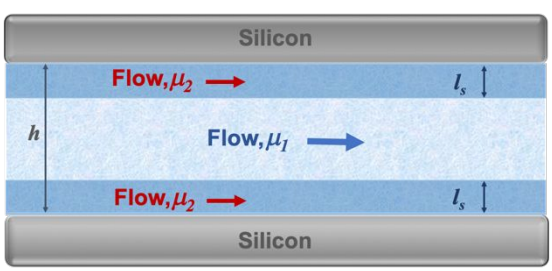

Figure 1. The schematic of the interfacial layer developed in nanochannels with a viscosity (μ_2) greater than that of the bulk liquid (μ_1).

Assume μ_2 to be the apparent viscosity of the thin liquid layer with a thickness l_s next to the nanochannel wall that differs from that in the bulk μ_1 (Figure 1). The liquid, hence, moves with different velocities, i.e., u_2 and u_1, respectively, according to Navier-Stokes equation:

$$\mu_1 \frac{\partial^2 u_1}{\partial z^2} - \frac{dp}{dx} = 0 \tag{2a}$$

$$\mu_2 \frac{\partial^2 u_2}{\partial z^2} - \frac{dp}{dx} = 0 \tag{2b}$$

where p is the liquid pressure, and x and z represent the coordinates along the flow and channel height directions, respectively. Integrating Eqs. (2a) and (2b) and applying appropriate boundary conditions yields (see Supporting Information, S1)

$$u_1 = \frac{1}{\mu_1}\left(\frac{dp}{dx}\right)\frac{z^2}{2} - \frac{1}{\mu_2}\left(\frac{dp}{dx}\right)\frac{h^2}{8} - \left(\frac{dp}{dx}\right)\left(\frac{1}{\mu_1} - \frac{1}{\mu_2}\right)\left(\frac{l_s^2}{2}\right) \tag{3a}$$

$$u_2 = \frac{1}{\mu_2}\left(\frac{dp}{dx}\right)\frac{z^2}{2} - \frac{1}{\mu_2}\left(\frac{dp}{dx}\right)\frac{h^2}{8} \tag{3b}$$

where h represents the channel height.

Mass flow rate $\dot{m}$ in the channel can be obtained as

$$\dot{m} = 2\rho w\left(\int_0^{l_s} u_1 dz + \int_{l_s}^{\frac{h}{2}} u_2 dz\right) \tag{4}$$

where ρ is the liquid density and w is the channel width. Substituting Eqs. (3a) and (3b) into Eq. (4) and integrating both sides yields

$$\dot{m} = 2\rho w\left(-\left(\frac{1}{\mu_1} - \frac{1}{\mu_2}\right)\left(\frac{l_s^3}{3}\right) - \frac{1}{\mu_2}\frac{h^3}{24}\right)\left(\frac{\Delta p}{x}\right) \tag{5}$$

where Δp represents the capillary pressure drop along the liquid-filled part of the channel, x.

On the other hand, $\dot{m}$ can be written as

$$\dot{m} = \rho w h \frac{dx}{dt} \tag{6}$$

Substituting Eq. (6) into Eq. (5) and performing an integration on both sides yields the following relationship between the liquid front position and time:

$$x^2 = \frac{4}{h}\Delta p\left(-\left(\frac{1}{\mu_1} - \frac{1}{\mu_2}\right)\left(\frac{l_s^3}{3}\right) - \frac{1}{\mu_2}\frac{h^3}{24}\right)t \tag{7}$$

Substituting $\Delta p = -2\gamma\kappa$ for capillary pressure in Eq. (7) yields

$$x = \sqrt{\left(\frac{8\gamma\kappa}{h}\right)\left(\left(\frac{1}{\mu_1} - \frac{1}{\mu_2}\right)\left(\frac{l_s^3}{3}\right) + \frac{1}{\mu_2}\frac{h^3}{24}\right)}\sqrt{t} \tag{8}$$

where κ denotes the mean curvature of the interface. For a 2D nanochannel with a height of h and a width of w and a liquid/wall contact angle of θ, we have $\kappa = \frac{1}{2}\left(\frac{1}{h} + \frac{1}{w}\right)\cos\theta$ [16].

It can be noticed that our governing equation for liquid displacement with time (Eq. (8)) still complies with the $x = K\sqrt{t}$ form proposed by LW equation, whereas for the nanochannels, the coefficient K must be replaced with K_{nc} expressed as:

$$K_{nc} = \sqrt{\left(\frac{8\gamma\kappa}{h}\right)\left(\left(\frac{1}{\mu_1} - \frac{1}{\mu_2}\right)\left(\frac{l_s^3}{3}\right) + \frac{1}{\mu_2}\frac{h^3}{24}\right)} \tag{9}$$

It can be seen that all the parameters needed to obtain K_{nc} according to Eq. (9) are known except for the interfacial viscous

layer thickness, l_s and the interfacial viscosity, μ_2. These values are determined through experimental results and are compared to the developed model, Eq. (8). In addition, experimental investigations of liquid flow in nanochannels with different heights as well as molecular dynamics (MD) shearing modeling confirm the applicability of the developed framework for flow in nanoscale conduits.

Experimental

Nanochannel Fabrication. Si nanochannels with heights of 20 nm, 40 nm and 80 nm were fabricated through a nanofabrication process discussed in the Supporting Information, S2. Each set of nanochannels includes 11 groups of channels with 9 parallel channels in each group. Channels were designed with a width of 5 μm. Each nanochannel extends between two large micro-reservoirs that are 20 μm deep. The profiles of different nanochannels were characterized via Scanning Probe Microspore (SPM) as shown in Figure 2 and their height uniformity was confirmed (Figure S2 in Supporting Information). Finally, the nanochannels were sealed on top with a borosilicate glass through anodic bonding.

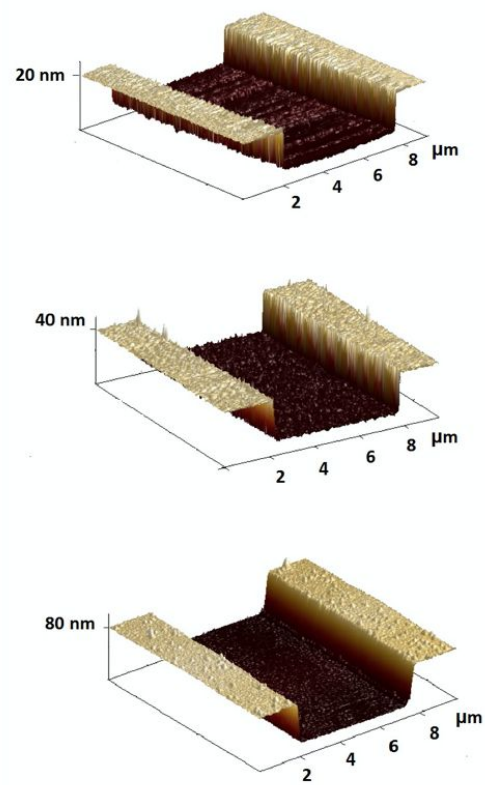

Figure 2. Uniform profiles of Si nanochannels with different heights probed with scanning probe microscopy (SPM).

Liquid Imbibition Visualization. The micro-nanofluidic chip was plasma cleaned (Harrick Plasma, PDC-001, Ithaca, NY) with Oxygen for 10 minutes before each run. The chip was then placed on an Eclipse LV100ND upright microscope stage (Nikon Metrology Inc., Brighton, MI). Afterward, the liquid was introduced to the device through the inlet of one of the reservoirs. Once the reservoir was filled, liquid started to penetrate the nanochannels due to capillarity. The liquid transport in the nanochannels was visualized through a Phantom V711 high-speed camera (Vision Research Inc., Wayne, NJ) coupled with the optical microscope system. Representative snapshots of capillary flow of IPA in nanochannels with different heights are shown in Figure 3. The liquid front (i.e., liquid/air interface) displacement in the nanochannels with respect to time was extracted by image-processing the captured videos using a developed MATLAB code [48]. Experiments were carried out for two types of organic liquids, i.e., isopropanol, also known as IPA, and ethanol. These liquids provide total wetting condition in the Si nanochannels. For each set of liquid and nanochannel height, a minimum of 10 experiments were performed and the results were averaged. The ambient temperature was maintained at 20℃ throughout the experiments via an active heating/cooling system.

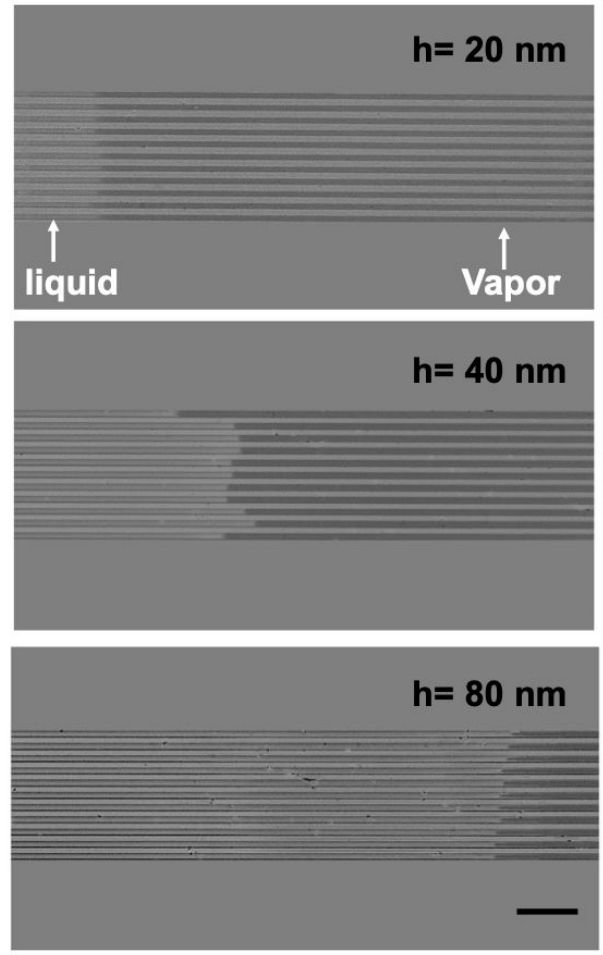

Figure 3. Snapshots from capillary flow of IPA in nanochannels with different heights (h) all taken 1.2 seconds after flow initiation demonstrate that liquid transport is significantly faster for nanochannel with larger heights. The scale bar is equal to 50 μm.

MD Simulation. In the simulations, the model consisting of 720 organic liquid molecules confined between two silica substrates as shown in Figure 4 was developed. The approximate dimensions of $7\ nm\ (x) \times 7\ nm\ (y) \times 1.5\ nm\ (z)$ were used for the silica substrates. Two different types of organic liquid molecules, i.e., C_3H_7OH (IPA) and C_2H_5OH (ethanol) were studied. Periodic boundary conditions were applied in the x and y directions. Since simulating channels wider than 10 nm is impractical for MD simulations due to the computational cost, the thickness of the IPA and ethanol liquid

layer for the simulation was around 2 *nm*. We indeed performed simulations on a larger channel height (3.5 nm) at a shear velocity of 100 m/s and found the calculated viscosity (1.18 mPaS) to be similar to that from the 2 nm case (1.11 mPaS). We thus chose to use the smaller system to calculate the apparent viscosity at other shear velocities.

The amorphous silica substrate was modeled using the BKS force field [49, 50]. The popular OPLS-AA force field [51, 52] was adopted to model the organic liquids. The non-bond interactions between silica and organic liquids were simulated using the following Lennard-Jones (L-J) interaction equation

$$E = 4\varepsilon\left[\left(\frac{\sigma}{r_{ij}}\right)^{12} - \left(\frac{\sigma}{r_{ij}}\right)^{6}\right] \qquad (10)$$

where ε and σ are the energy and length constants, respectively, and r_{ij} is the distance between two atoms, i and j. A cutoff of 1 nm was chosen for the L-J interactions.

The long-range electrostatic interaction in the entire system was computed by the PPPM (particle-particle particle-mesh) approach with an accuracy of 1×10^{-5}. Simulations were performed using the large-scale atomic/molecular massively parallel simulator (LAMMPS) [53] with a chosen time step of 1 fs.

First, the system was energy-minimized and equilibrated in a canonical ensemble (NVT) at 295 K for 0.5 ns. Then, the system was optimized in an isothermal-isobaric ensemble (NPT) at 1 atm and 295 K for another 2 ns. After the structures were fully relaxed, the top part of the silica substrate was sheared by translating the top slab at constant speeds of 100, 200, 400, 600 m/s, which corresponds to shear rates on the order of 10^{10}-10^{11}/s, similar to those used in other non-equilibrium molecular dynamics (NEMD) simulations [54, 55, 56, 57, 58, 59]. The viscous heat generated during the shearing simulations was dissipated using a thermostat acting on the relaxed portion of the silica substrate [60]. This indirect heat dissipation method can overcome the disadvantage of directly thermostating the fluid which perturbs liquid molecular dynamics [61, 62]. The Navier shear viscosity was calculated as $\mu = -S_{xz}/\dot{\gamma}$ where $\dot{\gamma}$ is the shear rate, and S_{xz} is the shear component (xz) of the stress tensor, which consists of the kinetic energy contribution and the virial term [63].

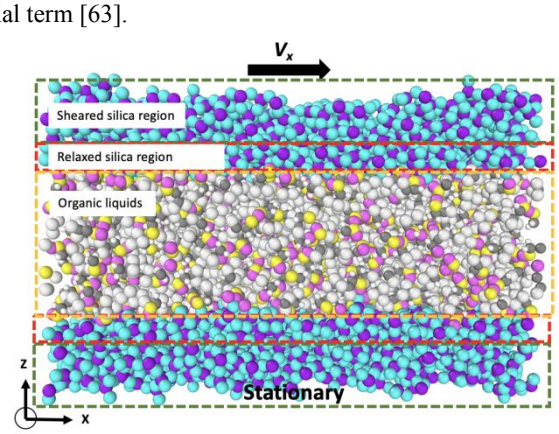

Figure 4. An example model setup for shearing simulations, where the relaxed silica region is thermostatted at 295 K during the shearing process to dissipate the viscous heat. The top silica substrate moves at different speeds in the x-direction.

Results and Discussion

Experimental Results. The capillary motion of IPA and ethanol inside the nanochannels of variable heights were monitored with respect to time. It was observed that liquid imbibition always follows a $x \propto \sqrt{t}$ relationship. However, the proportionality constant was significantly smaller than that predicted by LW equation (K). As shown in Figure 5, for all channel heights used in this study, significant deviations in IPA capillary flow kinetics between the experimentally obtained data and those predicted by LW equation were observed. Analogous behavior was observed in the imbibition of ethanol (see Figure S3 in Supporting Information). Figure 6 shows the deviations for different channel heights that were calculated as the difference in percentage between the slope predicted from LW equation (K) and slope of the linear regression fitted to each data set.

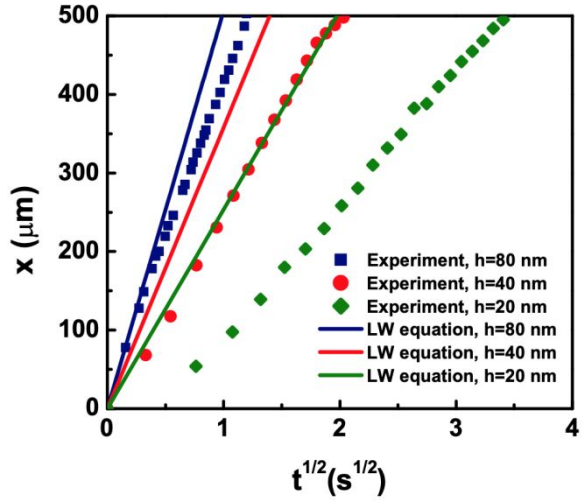

Figure 5. Comparison between LW model prediction and the experimental results for liquid meniscus position versus square root of time in nanochannels with different heights for capillary filling of IPA.

The divergence between the experimental observations and theoretical data based on LW equation increases for channels with smaller heights. As shown in Figure 6 the mismatch can become as large as 45% for the nanochannels with a height of 20 nm. In addition, LW equation error was greater in experiments with IPA compared to ethanol which implies that the effect of interfacial viscous layer is more pronounced in capillary flow of IPA. More explanation on this is provided in the remainder of this paper.

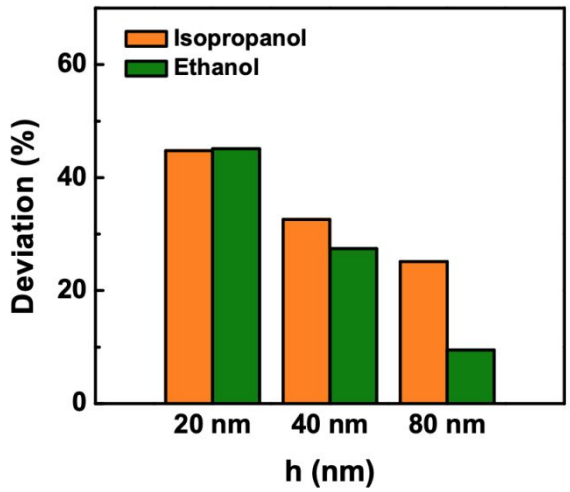

Figure 6. The deviation between the LW model and the experimental results for imbibition coefficient increases for channels with smaller heights.

Interfacial Viscous Layer Thickness Calculation. As discussed earlier, development of a several molecule-thick interfacial layer adjacent to the walls with a viscosity greater than the bulk slows the capillary filling in nanochannels. The yet unknown thickness of this layer l_s plays a critical role in determining the imbibition rate as expressed in Eq. (8). It must be noted that the radial distribution function profiles for both organic liquids (Figure S4 in Supporting Information) manifest strong layering effect near the walls. Hence, in accordance with previous studies [64, 65], l_s is presumed to take on values that are multiples of the liquid molecular size i.e., $l_s = nd$, where d represents the liquid molecular diameter. Two different analytical methods were employed to solve for l_s.

In the first approach, an initial guess for n was used to calculate l_s. Then, Eq. (8) was solved for μ_2 by substituting a datum point (x,t) from the experimental results for a $20\ nm$ tall channel. As the interfacial layer forms owing to the liquid/wall interactions, its thickness depends on liquid and channel material properties but remains insensitive to the channel height. Hence, the obtained l_s and μ_2 were, subsequently, substituted in Eq. (9) and K_{nc} values were calculated for channels with heights of 40 and $80\ nm$. For both $h = 40\ nm$ and $h = 80\ nm$, fitting of $x = K_{nc}\sqrt{t}$ to the experimental data was evaluated for the obtained K_{nc} value. This process was repeated for different input values for n. Eventually, the n value that produced the closest matches to the experimental data for all channel heights was adopted to calculate l_s.

In the second strategy, l_s was obtained by solving a system of equations for each liquid. By writing Eq. (8) for channels with 3 different heights, a system of equations was formed:

$$x - \sqrt{\left(\frac{8\gamma\kappa_{20}}{h_{20}}\right)\left(\left(\frac{1}{\mu_1} - \frac{1}{\mu_2}\right)\left(\frac{l_s^3}{3}\right) + \frac{1}{\mu_2}\frac{h_{20}^3}{24}\right)}\sqrt{t} = 0$$

$$x - \sqrt{\left(\frac{8\gamma\kappa_{40}}{h_{40}}\right)\left(\left(\frac{1}{\mu_1} - \frac{1}{\mu_2}\right)\left(\frac{l_s^3}{3}\right) + \frac{1}{\mu_2}\frac{h_{40}^3}{24}\right)}\sqrt{t} = 0 \qquad (11)$$

$$x - \sqrt{\left(\frac{8\gamma\kappa_{80}}{h_{80}}\right)\left(\left(\frac{1}{\mu_1} - \frac{1}{\mu_2}\right)\left(\frac{l_s^3}{3}\right) + \frac{1}{\mu_2}\frac{h_{80}^3}{24}\right)}\sqrt{t} = 0$$

where the subscripts for h and κ show the corresponding channel height. Note that to increase the reliability of the solution an overdetermined system of equations was formed and the number of equations exceeded the number of unknowns, i.e., μ_2 and l_s. Therefore, the solution was obtained by minimizing the Frobenius norm of the residual [66]. In addition, a constraint of $l_s = nd$ was imposed to limit the interfacial layer thickness to only take on values that are multiples of the liquid molecular size. By substituting three data points (x,t) from experiments in channels with heights of 20, 40 and $80\ nm$, respectively, the system of Eqs. (11) was solved and l_s was obtained.

As expected, both methods resulted in identical solutions for l_s for both IPA and ethanol. Our results indicated that $n = 4$ produces the closest match to the experimental data for imbibition of IPA, whereas the best match for ethanol was obtained for $n = 12$. Since the molecular sizes for IPA and ethanol are $d_{IPA} = 1.605\ nm$ and $d_{ethanol} = 0.44\ nm$, the obtained n values correspond to $l_s = 6.42\ nm$ and $l_s = 5.28\ nm$ for IPA and ethanol, respectively. Figure 7 depicts the experimental data for imbibition of IPA in a $40\ nm$ channel and the generated theoretical results based on Eq. (8) for several n values. Utilizing the definition of coefficient of determination (COD) the goodness of fits was evaluated and $n = 4$ was confirmed to yield the closest agreement with the experiment. Figure S5 in Supporting Information also shows the experimental data for capillary filling of ethanol in a $40\ nm$ tall channel where $n = 12$ generated the closest match. In addition, as shown in Figure 8, for both IPA and ethanol, the obtained n values resulted in close agreement between the model and the experimental data for all channel heights. The small deviations between the model and the experimental data for 20 nm channels are attributed to changes in the effective channel height after anodic bonding. In fact, the electrostatic interactions undergone during the anodic bonding of silicon and glass are sufficiently strong to induce small deformations and decrease the effective height of the channel compared to the 20 nm height measured prior to the bonding and cause small changes in filling rate.

The obtained l_s values also explain the difference in deviations between the experiments and LW equation observed for IPA and ethanol in Figure 6. In fact, the larger thickness of IPA interfacial layer compared to ethanol ($6.42\ nm$ versus $5.28\ nm$) results in a more significant contribution of this effect to the kinetics of the overall process. Therefore, since LW equation does not consider the interfacial layer effect, its deviations from experiments increases for flow of IPA.

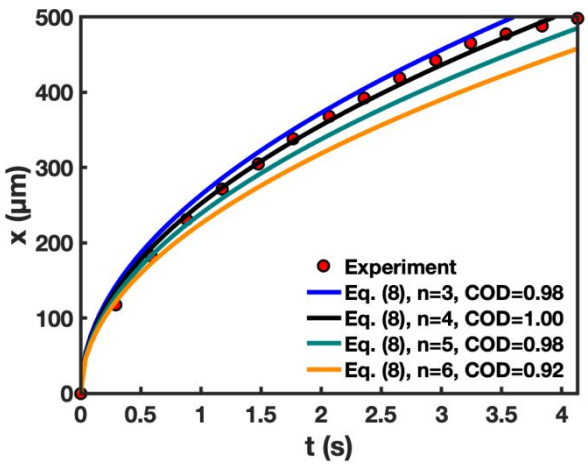

Figure 7. The COD values show that n=4 yields the closest match between our model and the experimental data for imbibition of IPA in 40 nm channel.

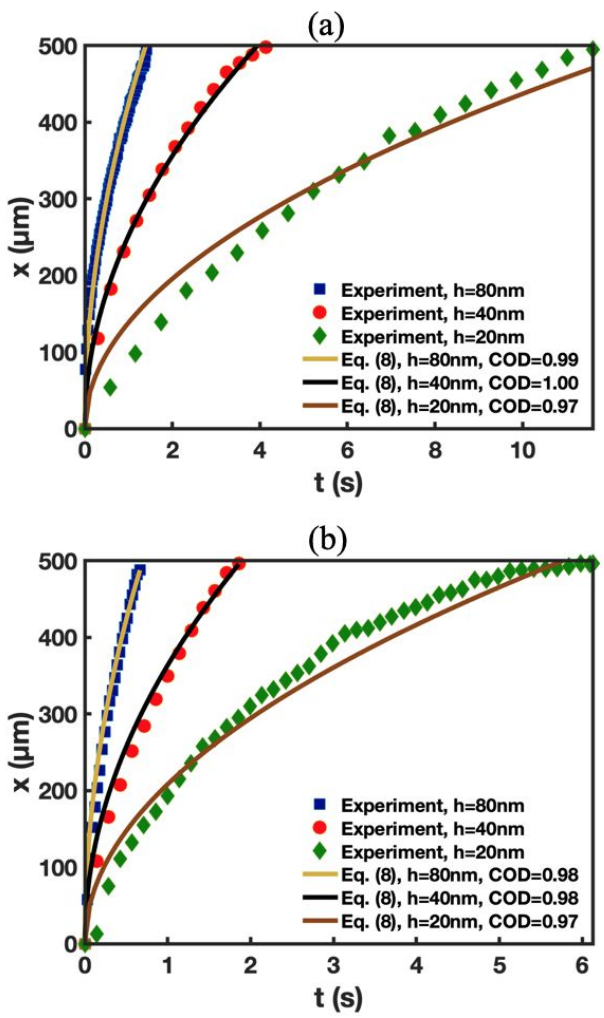

Figure 8. The predicted results show close agreement with the experimental data for all channel heights for (a) IPA and (b) ethanol.

Interfacial Viscosity Calculation. As discussed earlier, the liquid viscosity within the interfacial layer adjacent to the walls, μ_2 is larger than that in the bulk, μ_1. Either by solving the system of equations shown in (11) for each liquid, or following the first approach described in previous section, μ_2 values can be obtained as one of the unknowns. Table 1 shows the calculated μ_2 values along with the reference values of μ_1 for both IPA and ethanol [67].

Table 1. Comparison between the theoretically obtained interfacial viscosities of two organic liquids studied in this work and their reference bulk viscosities at 20℃ and 1 atm.

Liquid	μ_1(mPa.s)	μ_2(mPa.s)	Difference (%)
IPA	2.390	9.048	279%
Ethanol	1.173	4.405	276%

It can be seen that IPA and ethanol experience a 279% and a 276% increase in viscosity adjacent to the channel walls, respectively. This increase in viscosity can be attributed to the van der Waals and electrostatic interactions at the liquid/wall interface.

Shear viscosities for both IPA and ethanol were calculated through NEMD simulations, as well. The NEMD method is chosen for shear viscosity calculation due to its robustness compared to equilibrium molecular dynamics simulations (such as Green-Kubo formula) that generally suffer from thermal fluctuation-induced noise in the auto correlation function. Several different shear velocities (V_S) ranging from 10 to 100 m/s were used, and the calculated shear viscosities are shown in Figure 9. It is known that shear-thinning behavior (shear viscosity decreasing with shear rate) can happen for both IPA and ethanol as reported previously [68]. However, due to the time (~ns) and length (~nm) scales of the MD simulations, the shear rate in the simulation is much higher (10^{10}-10^{11}/s) than that in the experiments (~10^4/s). Thus, for a fair comparison with experiments, interfacial viscosity should be obtained by extrapolating the NEMD results to the low shear velocity limit. We fitted the NEMD data by applying the Carreau-Yasuda relationship [69, 70]:

$$\mu = \mu_0 \left[1 + (\lambda V_s)^a\right]^{(n-1)/a} \qquad (12)$$

where λ is a constant with a unit of $(m/s)^{-1}$ and n and a are dimensionless constants. μ_0 $(Pa.s)$ is the Newtonian viscosity, i.e., the liquid viscosity at zero shear rate. This model predicts a constant viscosity at low shear velocities that transitions to shear-thinning as the shear exceeds a certain threshold.

Final shear viscosities of the liquids were obtained by evaluating μ values of the fitted regression at $V_s = 0$. The plateau shown in the inset of Figure 9 represents the constant viscosity region at low shear rates for both liquids. We note that since the channel height of 2 nm in the simulations is smaller than the estimated interfacial layer thickness, the predicted viscosity is mainly influenced by the liquid/wall interaction and should be compared to the interfacial viscosity, μ_2, in Table 1. The calculated viscosities for both liquids are in close agreement with the experimentally obtained interfacial viscosity values, as demonstrated in Figure 10.

It must be added that while liquid slippage in hydrophobic nanochannels is common, the confined liquid velocity profiles obtained from NEMD simulations (Figure S6 in Supporting Information) show no flow slippage during the filling process.

This can be justified considering the strong affinity between the organic liquids and silicon walls.

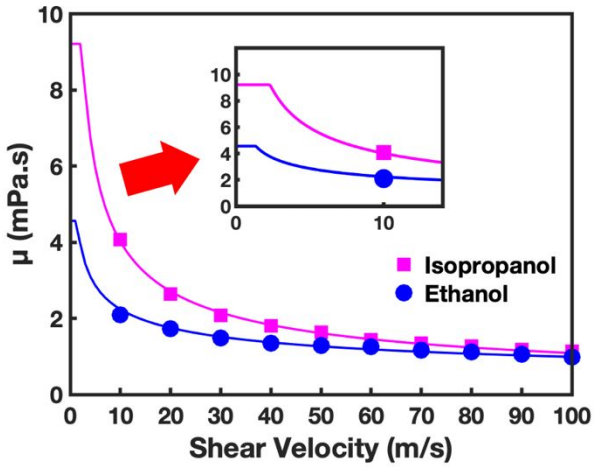

Figure 9. The shear viscosity values for isopropanol and ethanol at different shear velocities obtained from NEMD simulations and the analytical fit to the data.

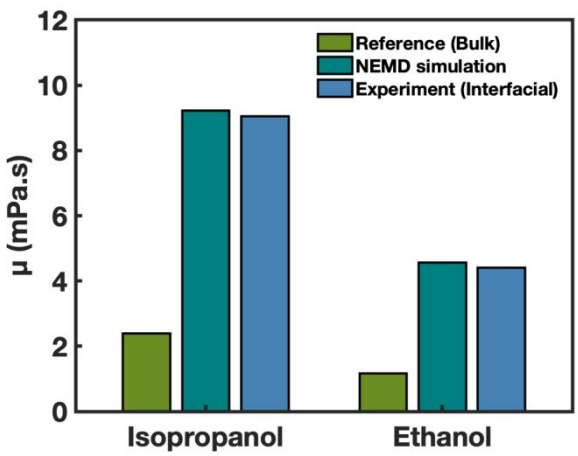

Figure 10. Bulk viscosity of IPA and ethanol compared with their interfacial viscosity values obtained through numerical simulation and our theoretical model solution.

In conclusion, in this study we proposed a theoretical model for capillary flow in nanoscale conduits as the well-known Lucas-Washburn equation has been confirmed to be incapable of predicting the liquid flow kinetics in channels with nanoscopic heights. Our model incorporated the interfacial viscosity effect on the kinetics of liquid imbibition in nanochannels and was able to successfully predict the capillary flow rates for different liquids in channels with different heights as compared against experimental observations. In fact, we illustrated that the increased viscosity in a several molecule-thick layer adjacent to the walls is the primary reason for the lower rates of capillary motion observed in nanoscopic channels. MD simulations were also conducted and shear viscosities of the liquids studied in this work were obtained through NEMD, which matched the experimental results very well. The close agreement between the results from the experimental data based on our model and the numerical simulations underscores the role of interfacial viscosity in capillarity slowdown in nanochannels and clarifies the underlying physical phenomena responsible for the slow filling in nanochannels.

ASSOCIATED CONTENT

Supporting Information

The Supporting Information is available free of charge on the ACS Publications website. (Microsoft document)

S1: Applying Boundary Condition for the Governing Equations of Capillary Flow. S2: Nanochannel Fabrication. Figure S11: Fabrication process of Nanofluidic device. (a) Silicon wafer, (b) Spin coated photoresist on top of the Silicon wafer, (c) Nanochannels pattern on the positive photoresist through standard photolithography, (d) Etched Nanochannels on the silicon wafer through RIE, (e) Washed sample after etching, (f) Spin coated photoresist for a reservoir fabrication, (g) Micro-reservoirs pattern through standard photolithography, (h) Etched micro-reservoirs on the silicon wafer through RIE, (i) Washed sample after etching, (j) Growth of thermal oxide on the fabricated micro-nanochannels, (k) Sealed micro-nanochannel with glass through anodic bonding. Figure S2: Height profile analysis of nanochannels obtained by Scanning Probe Microscopy. Height uniformity across the nanochannels with heights of (a) 20 nm, (b) 40 nm and (c) 80 nm is confirmed. Figure S3: The deviation of the LW model prediction from the experimental observation for imbibition of *ethanol* in nanochannels with heights of 80 nm, 40 nm, *and* 20 nm. Figure S4: The COD values show that n=12 yields the closest match between our model and the experimental data for imbibition of ethanol in 40 nm channel.

AUTHOR INFORMATION

Corresponding Author

Hadi Ghasemi - *Department of Mechanical Engineering, University of Houston,*
Email: hghasemi@uh.edu

Tengfei Luo - Department of Aerospace and Mechanical Engineering, University of Notre Dame,

Email: tluo@nd.edu

Author Contributions

The manuscript was written through contributions of all authors. / All authors have given approval to the final version of the manuscript. / ‡These authors contributed equally.

Acknowledgement

The authors gratefully acknowledge funding support from the Air Force Office of Scientific Research (AFOSR) for grant FA9550-16-1-0248 with Dr. Ali Sayir as program manager. The authors thank Drs. Long Chang and Jing Guo in the nanofabrication facility at University of Houston and Dr. Marylene Palard at University of Texas-Austin supported by NSF grant NNCI-1542159 for their help on the development of nanochannels.

ABBREVIATIONS

LW, Lucas-Washburn; L-J, Lennard-Jones; MD, molecular dynamics; NEMD, non-equilibrium molecular dynamics; PPPM, particle-particle particle-mesh; COD, coefficient of Determination;

REFERENCES

[1] Wheeler, T.D. and Stroock, A.D., "The transpiration of water at negative pressures in a synthetic tree," *Nature,* pp. 208-212, 2008.

[2] Ha, J., Kim, J., Jung, Y., Yun, G., Kim, D.N. and Kim, H.Y., "Poro-elasto-capillary wicking of cellulose sponges," *Science advances,* p. eaao7051, 2018.

[3] Wang, Y., Lee, J., Werber, J.R. and Elimelech, M., "Capillary-driven desalination in a synthetic mangrove," *Science Advance,* p. eaax5253, 2020.

[4] Shi, Weiwei, Joshua R. Vieitez, Austin S. Berrier, Matthew W. Roseveare, Daniel A. Surinach, Bernadeta R. Srijanto, C. Patrick Collier, and Jonathan B. Boreyko, "Self-stabilizing transpiration in synthetic leaves," *ACS applied materials & interfaces* , pp. 13768-13776, 2019.

[5] Koos, E. and Willenbacher, N., "Capillary forces in suspension rheology," *Science,* pp. 897-900, 2011.

[6] Bocquet, L., Charlaix, E., Ciliberto, S. and Crassous, J., "Moisture-induced ageing in granular media and the kinetics of capillary condensation," *Nature,* pp. 735-737, 1998.

[7] Choi, J., Ghaffari, R., Baker, L.B. and Rogers, J.A., "Skin-interfaced systems for sweat collection and analytics," *Science advances,* p. eaar3921, 2018.

[8] Sinha, P.M., Valco, G., Sharma, S., Liu, X. and Ferrari, M., "Nanoengineered device for drug delivery application," *Nanotechnology,* p. S585, 2004.

[9] Hamblin, M.N., Xuan, J., Maynes, D., Tolley, H.D., Belnap, D.M., Woolley, A.T., Lee, M.L. and Hawkins, A.R., "Selective trapping and concentration of nanoparticles and viruses in dual-height nanofluidic channels," *Lab on a Chip,* pp. 173-178, 2010.

[10] Kamitani, A., Morishita, S., Kotaki, H. and Arscott, S., "Microfabricated microfluidic fuel cells," *Sensors and Actuators B,* pp. 174-180, 2011.

[11] Storm, M.M., Johnsen, R.E., Younesi, R. and Norby, P., "Capillary based Li-air batteries for in situ synchrotron X-ray powder diffraction studies," *Journal of Materials Chemistry A,* pp. 3113-3119, 2015.

[12] Davoodabadi, Ali, Jianlin Li, Yongfeng Liang, David L. Wood III, Timothy J. Singler, and Congrui Jin., "Analysis of electrolyte imbibition through lithium-ion battery electrodes.," *Journal of Power Sources,* pp. 193-203, 2019.

[13] Gostick, Jeff T., Marios A. Ioannidis, Michael W. Fowler, and Mark D. Pritzker. , "Wettability and capillary behavior of fibrous gas diffusion media for polymer electrolyte membrane fuel cells.," *Journal of Power Sources,* pp. 433-444, 2009.

[14] Liu, S., Pu, Q., Gao, L., Korzeniewski, C. and Matzke, C., "From nanochannel-induced proton conduction enhancement to a nanochannel-based fuel cell," *Nano Letters,* pp. 1389-1393, 2005.

[15] Cho, H. Jeremy, Daniel J. Preston, Yangying Zhu, and Evelyn N. Wang. , "Nanoengineered materials for liquid-vapour phase-change heat transfer," *Nature Reviews Materials 2,* pp. 1-17, 2016.

[16] Nazari, Masoumeh, Ali Masoudi, Parham Jafari, Peyman Irajizad, Varun Kashyap, and Hadi Ghasemi., "Ultrahigh evaporative heat fluxes in nanoconfined geometries.," *Langmuir,* pp. 78-85, 2018.

[17] Li, Jiaqi, Wuchen Fu, Bohan Zhang, Gaohua Zhu, and Nenad Miljkovic, "Ultrascalable Three-Tier Hierarchical Nanoengineered Surfaces for Optimized Boiling," *ACS nano,* 2019.

[18] Jafari, Parham, Ali Masoudi, Peyman Irajizad, Masoumeh Nazari, Varun Kashyap, Bahareh Eslami, and Hadi Ghasemi, "Evaporation Mass Flux: A Predictive Model and Experiments," *Langmuir* , pp. 11676-11684, 2018.

[19] Farokhnia, Nazanin, Seyed Mohammad Sajadi, Peyman Irajizad, and Hadi Ghasemi, "Decoupled hierarchical structures for suppression of Leidenfrost phenomenon," *Langmuir,* pp. 2541-2550, 2017.

[20] Farokhnia, Nazanin, Peyman Irajizad, Seyed Mohammad Sajadi, and Hadi Ghasemi, "Rational micro/nanostructuring for thin-film evaporation," *The Journal of Physical Chemistry C,* pp. 8742-8750, 2016.

[21] Xue, Y., Markmann, J., Duan, H., Weissmüller, J. and Huber, P., "Switchable imbibition in nanoporous gold," *Nature communications,* pp. 1-8, 2014.

[22] Bao, Bo, Seyed Hadi Zandavi, Huawei Li, Junjie Zhong, Arnav Jatukaran, Farshid Mostowfi, and David Sinton, "Bubble nucleation and growth in nanochannels," *Physical Chemistry Chemical Physics,* pp. 8223-8229, 2017.

[23] Kim, S.J., Ko, S.H., Kang, K.H. and Han, J., "Direct seawater desalination by ion concentration polarization," *Nature nanotechnology,* pp. 297-301, 2010.

[24] Han, J. and Craighead, H.G., "Separation of long DNA molecules in a microfabricated entropic trap array," *Science,* pp. 1026-1029, 2000.

[25] Esfandiar, A., Radha, B., Wang, F.C., Yang, Q., Hu, S., Garaj, S., Nair, R.R., Geim, A.K. and Gopinadhan, K., "Size effect in ion transport through angstrom-scale slits," *Science,* pp. 511-513, 2017.

[26] Xie, Q., Alibakhshi, M.A., Jiao, S., Xu, Z., Hempel, M., Kong, J., Park, H.G. and Duan, C., "Fast water transport in graphene nanofluidic channels," *Nature nanotechnology,* pp. 238-245, 2018.

[27] Washburn, E.W., "The dynamics of capillary flow," *Physical review,* p. 273, 1921.

[28] Lucas, R., "Rate of capillary ascension of liquids," *Kolloid Z,* pp. 15-22, 1918.

[29] Alibakhshi, Mohammad Amin, Quan Xie, Yinxiao Li, and Chuanhua Duan., "Accurate measurement of liquid transport through nanoscale conduits.," *Scientific reports,* p. 24936, 2016.

[30] Cheng, J.T. and Giordano, N., "Fluid flow through nanometer-scale channels," *Physical review E,* p. 031206, 2002.

[31] Yang, D., Krasowska, M., Priest, C., Popescu, M.N. and Ralston, J., "Dynamics of capillary-driven flow in open microchannels," *The Journal of Physical Chemistry C,* pp. 18761-18769, 2011.

[32] Han, A., Mondin, G., Hegelbach, N.G., de Rooij, N.F. and Staufer, U., "Filling kinetics of liquids in nanochannels as narrow as 27 nm by capillary force," *Journal of Colloid and Interface Science,* pp. 151-157, 2006.

[33] Persson, F., Thamdrup, L.H., Mikkelsen, M.B.L., Jaarlgard, S.E., Skafte-Pedersen, P., Bruus, H. and Kristensen, A., "Double thermal oxidation scheme for the fabrication of SiO2 nanochannels," *Nanotechnology,* p. 245301, 2007.

[34] Tas, N.R., Haneveld, J., Jansen, H.V., Elwenspoek, M. and van den Berg, A., "Capillary filling speed of water in nanochannels," *Applied Physics Letters,* pp. 3274-3276, 2004.

[35] Thamdrup, L.H., Persson, F., Bruus, H., Kristensen, A. and Flyvbjerg, H., "Experimental investigation of bubble formation during capillary filling of Si O 2 nanoslits," *Applied Physics Letters,* p. 163505, 2007.

[36] Haneveld, J., Tas, N.R., Brunets, N., Jansen, H.V. and Elwenspoek, M., "Capillary filling of sub-10 nm nanochannels," *Journal of applied physics,* p. 014309, 2008.

[37] Mortensen, N.A. and Kristensen, A., "Electroviscous effects in capillary filling of nanochannels," *Applied Physics Letters,* p. 063110, 2008.

[38] Yang, M., Cao, B.Y., Wang, W., Yun, H.M. and Chen, B.M., "Experimental study on capillary filling in nanochannels," *Chemical Physics Letters,* pp. 137-140, 2106.

[39] Oh, J.M., Faez, T., de Beer, S. and Mugele, F., "Capillarity-driven dynamics of water-alcohol mixtures in nanofluidic channels," *Microfluidics and nanofluidics,* pp. 123-129, 2010.

[40] Chauvet, F., Geoffroy, S., Hamoumi, A., Prat, M. and Joseph, P., "Roles of gas in capillary filling of nanoslits," *Soft Matter,* pp. 10738-10749, 2012.

[41] Cao, B.Y., Chen, M. and Guo, Z.Y., "Liquid flow in surface-nanostructured channels studied by molecular dynamics simulation," *Physical Review E,* p. 066311, 2006.

[42] Ma, Y., Xue, S., Hsu, S.C., Yeh, L.H., Qian, S. and Tan, H., "Programmable ionic conductance in a pH-regulated gated nanochannel," *Physical Chemistry Chemical Physics,* pp. 20138-20146, 2014.

[43] Feng, D., Li, X., Wang, X., Li, J. and Zhang, X., "Capillary filling under nanoconfinement: The relationship between effective viscosity and water-wall interactions," *International Journal of Heat and Mass Transfer,* pp. 900-910, 2018.

[44] Phan, V.N., Yang, C. and Nguyen, N.T., "Analysis of capillary filling in nanochannels with electroviscous effects," *Microfluidics and Nanofluidics,* p. 519, 2009.

[45] Phan, V.N., Joseph, P., Djeghlaf, L., Allouch, A.E.D., Bourrier, D., Abgrall, P., Gue, A.M., Yang, C. and Nguyen, N.T., "Capillary Filling in Nanochannels—Modeling, Fabrication, and Experiments," *Heat Transfer Engineering,* pp. 624-635, 2011.

[46] Oyarzua, E., Walther, J.H., Mejia, A. and Zambrano, H.A., "Early regimes of water capillary flow in slit silica nanochannels," *Physical Chemistry Chemical Physics,* pp. 14731-14739, 2015.

[47] Zhong, J., Alibakhshi, M.A., Xie, Q., Riordon, J., Xu, Y., Duan, C. and Sinton, D., "Exploring Anomalous Fluid Behavior at the Nanoscale: Direct Visualization and Quantification via Nanofluidic Devices," *Accounts of Chemical Research,* 2020.

[48] "MATLAB R2019a," The Mathworks, Inc., [Online]. Available: www.mathworks.com/. [Accessed 02 05 2019].

[49] Tangney, P. and Scandolo, S., "An ab initio parametrized interatomic force field for silica," *The Journal of chemical physics,* pp. 8898-8904, 2002.

[50] Van Beest, B.W.H., Kramer, G.J. and Van Santen, R.A., "Force fields for silicas and aluminophosphates based on ab initio calculations," *Physical Review Letters,* p. 1955, 1990.

[51] Siu, S.W., Pluhackova, K. and Böckmann, R.A., "Optimization of the OPLS-AA force field for long hydrocarbons," *Journal of chemical theory and computation,* pp. 1459-1470, 2012.

[52] Jorgensen, W.L., Maxwell, D.S. and Tirado-Rives, J., "Development and testing of the OPLS all-atom force field on conformational energetics and properties of organic liquids," *Journal of the American Chemical Society,* pp. 11225-11236, 1996.

[53] Plimpton, S., "Fast parallel algorithms for short-range molecular dynamics," *Sandia National Labs,* 1993.

[54] Wagemann, E., Oyarzua, E., Walther, J.H. and Zambrano, H.A., "Slip divergence of water flow in graphene nanochannels: the role of chirality," *Physical Chemistry Chemical Physics,* pp. 8646-8652, 2017.

[55] Pahlavan, A.A. and Freund, J.B., "Effect of solid properties on slip at a fluid-solid interface," *Physical Review E,* p. 021602, 2011.

[56] Yong, X. and Zhang, L.T., "Slip in nanoscale shear flow: mechanisms of interfacial friction," *Microfluidics and nanofluidics,* pp. 299-308, 2013.

[57] Ashurst, W.T. and Hoover, W.G., "Argon shear viscosity via a Lennard-Jones potential with equilibrium and nonequilibrium molecular dynamics," *Physical Review Letters,* p. 206, 1973.

[58] Varnik, F. and Binder, K., "Shear viscosity of a supercooled polymer melt via nonequilibrium molecular dynamics simulations," *The Journal of chemical physics,* pp. 6336-6349, 2002.

[59] Priezjev, N.V., "Shear rate threshold for the boundary slip in dense polymer films," *Physical Review E,* p. 031608, 2009.

[60] Ewen, J.P., Kannam, S.K., Todd, B.D. and Dini, D., "Slip of alkanes confined between surfactant monolayers adsorbed on solid surfaces," *Langmuir,* pp. 3864-3873, 2018.

[61] Martini, A., Hsu, H.Y., Patankar, N.A. and Lichter, S., "Slip at high shear rates," *Physical review letters,* p. 206001, 2008.

[62] Bernardi, S., Todd, B.D. and Searles, D.J., "Thermostating highly confined fluids," *The Journal of chemical physics,* p. 244706, 2010.

[63] Huang, Dezhao, Teng Zhang, Guoping Xiong, Linji Xu, Zhiguo Qu, Eungkyu Lee, and Tengfei Luo, "Tuning Water Slip Behavior in Nanochannels using Self-Assembled Monolayers.," *ACS applied materials & interfaces,* pp. 32481-32488, 2019.

[64] Israelachvili, Jacob N., Patricia M. McGuiggan, and Andrew M. Homola, "Dynamic properties of molecularly thin liquid films.," *Science,* vol. 240, no. 4849, pp. 189-191, 1988.

[65] Thompson, Peter A., and Mark O. Robbins, "Origin of stick-slip motion in boundary lubrication.," *Science,* vol. 250, pp. 792-794, 1990.

[66] Horn, R.A. and Johnson, C.R., "Norms for vectors and matrices," *Matrix analysis,* pp. 313-386, 1990.

[67] Lide, D.R., CRC handbook of chemistry and physics: a ready-reference book of chemical and physical data, CRC press, 1995.

[68] Petravic, J. and Delhommelle, J., "Hydrogen bonding in ethanol under

shear," *The Journal of chemical physics,* p. 234509, 2005.

[69] McCabe, Clare, Charles W. Manke, and Peter T. Cummings, "Predicting the Newtonian viscosity of complex fluids from high strain rate molecular simulations," *The Journal of chemical physics,* pp. 3339-3342, 2002.

[70] Heyes, D. M., D. Dini, and E. R. Smith, "Incremental viscosity by non-equilibrium molecular dynamics and the Eyring model," *The Journal of chemical physics,* p. 194506, 2018.

[71] Doig, M., Warrens, C.P. and Camp, P.J., "Structure and friction of stearic acid and oleic acid films adsorbed on iron oxide surfaces in squalane," *Langmuir,* pp. 186-195, 2014.